INT. J. REMOTE SENSING, 20 NOVEMBER, 2003,
VOL. 24, NO. 22, 4433–4445

Taylor & Francis
Taylor & Francis Group

# Oakwood crown closure estimation by unmixing Landsat TM data

R. PU*, B. XU and P. GONG

Center for Assessment and Monitoring of Forest and Environmental Resources (CAMFER), 145 Mulford Hall, University of California, Berkeley, CA 94720-3114, USA

(*Received 15 May 2001; in final form 18 November 2002*)

**Abstract.** Using an unconstrained least squares solution (LSS) method and an artificial neural network (ANN) algorithm, we estimated oakwood crown closure from a Landsat Thematic Mapper (TM) image of Tulare County, California, USA. Fractions of endmembers (oak crown (f1), grass (f2) and soil (f3)) from mixed pixels were derived from aerial photographs (scale 1 : 40 000) scanned at 1 m ground resolution for training and testing the LSS and ANN algorithms. The aerial photographs were orthorectified using a digital photogrammetric software package with ground control points collected through a differential global positioning system (GPS). The TM image was georeferenced with respect to the corresponding orthorectified aerial photographs. The training and test samples were randomly selected from the TM image and their corresponding fractions of endmembers were derived from the orthophoto. A fourth endmember, shade (f4), was directly extracted from the TM image. Experimental results indicate that the ANN has performed better than the unconstrained LSS. To extract oakwood crown closure in mixed pixels, better results were obtained without using a shade endmember.

## 1. Introduction

Three million hectares of oakwood land in California have been changed over the last several decades (Standiford 1999). As might be expected in a state as ecologically diverse as California, oakwood land supports at least a dozen major tree species, predominantly of the genus *Quercus*, and many shrub and herbaceous species that occur in a myriad of combinations (Bartolome 1987, Allen *et al.* 1991). Tree crown closure is the percentage of forest canopy projected to a horizontal plane over a unit ground area (Avery and Burkhart 1994). Accurate estimation of crown closure of various oakwood species is a key technique for change detection of hardwood rangelands. Its measurement in the field is time consuming (Bonham 1989). Airphoto interpretation is employed as an alternative to oakwood classification and tree crown closure estimation. However, photo interpretation is dependent on the experience of photo interpretators (Biging *et al.* 1991, Gong and Chen 1992, Davis *et al.* 1995) and needs intensive human involvement. Recently, Gong *et al.* (2000) developed a photogrammetric approach to measure crown closure and tree height with greater accuracy. For large areas, however, it is expensive.

*Corresponding author; e-mail: rpu@nature.berkeley.edu

*International Journal of Remote Sensing*
ISSN 0143-1161 print/ISSN 1366-5901 online © 2003 Taylor & Francis Ltd
http://www.tandf.co.uk/journals
DOI: 10.1080/0143116031000095989

Satellite image (e.g. Landsat sensor imagery) classification as an information extraction tool has been used for more than three decades. Conventional classification techniques assume that all image pixels are pure. This assumption is often untenable with pixels of mixed land cover composition abundant in an image (Foody 1996). Consequently, conventional 'hard' image classification techniques only provide a poor base for the estimation of the area extent of land cover classes because any pixel is forced to belong to a single class. Therefore, it is desirable to decompose pixels into their components when their sizes are smaller than the pixel size. For this purpose, spectral mixture models and their inversion have been proposed (e.g. Adams *et al.* 1986, Blunt *et al.* 1990, Gong *et al.* 1994, Bowers and Rowan 1996, Ferrier and Wadge 1996, Sohn and McCoy 1997, McGwire *et al.* 2000). Among these, a linear spectral mixture model (LSM) was extensively applied to extract the abundance of various components within mixed pixels.

In LSM, the spectral signature of the mixed pixel is assumed to be a linear combination of spectral signatures of surface materials, called endmembers, components or cover types with their areal proportions as weighting factors (Gong and Zhang 1999). The basic physical assumption underlying the LSM is that there is no significant amount of multiple scattering between the different constituents; each photon that reaches the sensor has interacted with just one constituent (Settle and Drake 1993). The inversion of this problem is known as linear spectral unmixing. Nonlinear spectral mixture modelling can be found in Liang *et al.* (1991), Sasaki *et al.* (1983) and Zhang *et al.* (1998). In addition, an artificial neural network (ANN) algorithm has also been tested to unmix mixed pixels into fraction abundances of endmembers in some studies (Foody 1996, Wang and Zhang 1998). McGwire *et al.* (2000) quantified sparse vegetation cover information in arid environments using hyperspectral (Probe-1 data) mixture modelling and concluded that the use of a linear mixture model with multiple soil endmembers appeared to be the best method for quantifying sparse vegetation cover. Sohn and McCoy (1997) employed a spectral mixture modelling technique with Landsat Thematic Mapper (TM) data to map desert shrub rangeland and found that the linear unmixing could provide moderate estimates of vegetation fractions in arid rangeland. Ustin *et al.* (1992) applied linear unmixing to a hardwood rangeland to derive information about general endmembers, such as non-photosynthetic vegetation and green vegetation, using airborne visible/infrared imaging spectrometer (AVIRIS) images acquired from two seasons in a year. Smith *et al.* (1990) also applied linear unmixing to a Landsat TM image to determine desert scrub abundance.

Inversion of the LSM is easily performed once the spectra of endmembers are supplied. Endmember spectra can be taken from 'pure' pixels within an image, from spectral libraries of endmembers measured either in the laboratory or in the field, and from least squares estimation with pixel spectra and known abundances of endmembers. A number of automatic methods exist that identify endmember spectra through principal component analysis (Bateson and Curtiss 1996) and factor analysis (Evans *et al.* 1992). Most studies determining endmember spectra consider a set of known endmembers, derived from pure pixels or from libraries. However, even though a pixel area is covered by a single ground-cover type, its value may be different due to atmospheric disturbance and imperfect imaging process (Hu *et al.* 1999). In some areas, such as semi-arid and desert areas, it is

more difficult to get pure pixel values because vegetation is mixed with soil. Such difficulties can be overcome by measuring the fractions of endmembers from sample mixed pixels to allow for endmember spectra to be estimated for LSM. These measurements can also be used to train and test neural networks.

In this study, the LSM with an unconstrained least squares solution (LSS) and the error back-propagation and feed-forward ANN algorithm have been tested for oakwood crown closure extraction from Landsat TM data. We used interpretation results from orthorectified aerial photographs at 1 m ground resolution as ground data. After the Landsat TM image data at 30 m ground resolution were registered to the orthorectified aerial photographs, we calculated fractions of endmembers from the photo interpretation results for a sample of TM pixels. The major objective is to compare performances between LSS and ANN for extracting oakwood crown closure.

## 2. Study sites and data preparation

### 2.1. *Study site*

The study site is located at Three Rivers (TR, 58 $km^2$) in Tulare County, California, USA (figure 1). Oakwood crown closure in the study area is less than 25% and most TM pixels are mixtures of crown closure and other components such as grass, bare soil and a small percentage of shrub land. The sky in the summer months is usually crystal clear. Grasses are dead and dry. The reflectance of soil and dry grasses is higher than that of oak tree canopies in the visible bands but lower in the near-infrared bands of the TM imagery. The red colour in figure 1 shows crown coverage.

### 2.2. *Data preparation*

The Landsat TM imagery (path 041/row 035) for the study site was acquired on 16 August 1995 in the dry season. We used the original digital number (DN) of TM bands 1–5 and 7 with 30 m ground resolution in the spectral unmixing analysis. The mosaic aerial photographs were taken also in the dry season two months (4 October 1995) later than the satellite imagery. The aerial photographs (scale 1 : 40 000) were first scanned at approximately 1 m ground resolution. The scanned photographs were then orthorectified using a digital photogrammetric software

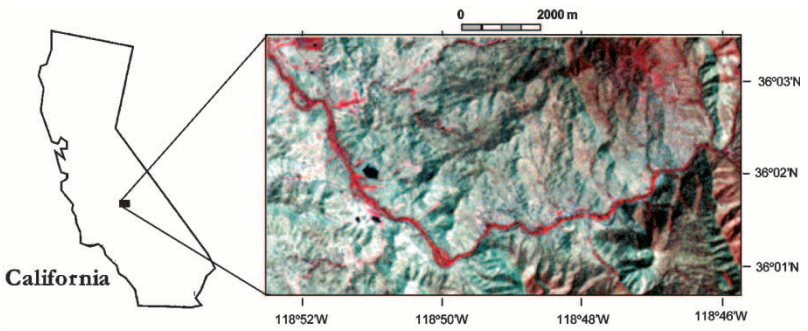


Figure 1. Landsat TM colour composites (RGB corresponding to TM bands 4, 3 and 2) showing the study site.

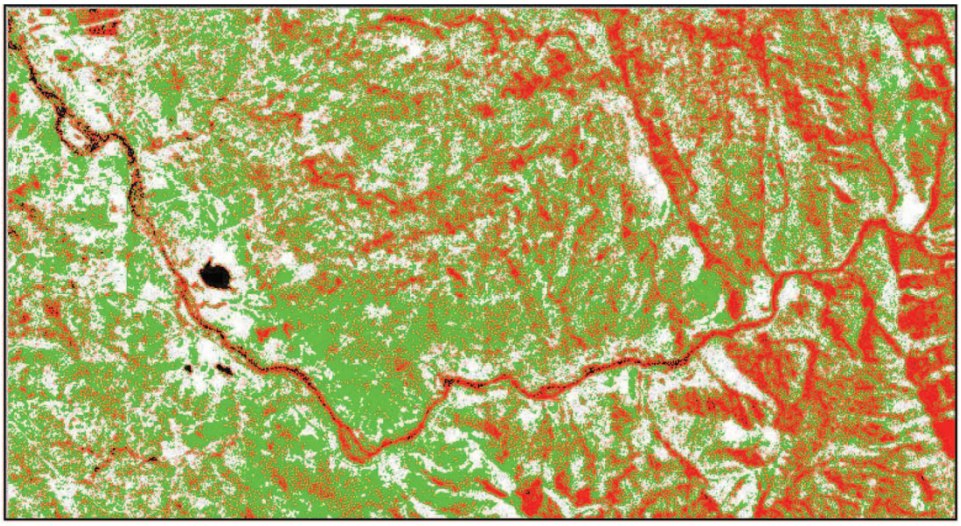

Figure 2. Interpretation results from aerial photographs for three endmembers. Crown (f1) presented in red, grasses (f2) in green and soil (f3) in grey.

package. Ground control points (GCPs) measured with geodetic precision global positioning system (GPS) equipment were used to derive the photographic stations and they were subsequently used in stereo model development and orthorectification in the Universal Transverse Mercator (UTM) projection (Gong *et al.* 2000). Since the resolution of the TM imagery was dramatically different from the aerial imagery, the TM data were carefully georeferenced with respect to the UTM projection on a 1 : 24 000-scale topographic map. The georeferencing accuracy was approximately 30 m. TM and orthophoto correspondence was carefully done through visual inspection guided by the UTM co-ordinates. Each pixel in the TM image corresponded to $30 \times 30$ pixels in the aerial photograph. In each 'transparent' mask (corresponding to one pixel) of the TM image over the $30 \times 30$ pixels of the aerial photograph, we were able to calculate the crown closure. Image thresholding was applied to derive land cover types from the orthophotos (figure 2). The average fractions of three endmembers were calculated and listed in table 1. No shaded area (f4) was calculated from the aerial photographs. The land cover results were used to calculate the percentages of endmembers for oak crown (f1), grass (f2) and soil (f3) for each corresponding pixel on the TM image. The shaded area (f4) was directly extracted from shadows of oak trees at shaded hillsides on the TM image.

Table 1. Interpretation results from aerial photographs for three endmember fractions (%) at the study site, California.

| Endmember | Fraction (%) |
|---|---|
| f1 (crown closure) | 26.91 |
| f2 (grasses) | 57.60 |
| f3 (soil) | 15.49 |

## 3. Methodology

A linear spectral mixing model at pixel ($i$, $j$) has four terms as presented in equation (1): a $K$-dimension digital-number vector, $\mathbf{DN}_{ij}$; an $L$-dimension fraction vector $\mathbf{F}_{ij}$; a $K \times L$ endmember spectra matrix $\mathbf{M}$; and $\boldsymbol{\varepsilon}_{ij}$, a $K$-dimension error vector representing residual error.

$$\mathbf{DN}_{ij} = \mathbf{M}\mathbf{F}_{ij} + \boldsymbol{\varepsilon}_{ij} \tag{1}$$

The goal of spectral unmixing is to solve for $\mathbf{F}_{ij}$ with $\mathbf{DN}_{ij}$ and $\mathbf{M}$ known. When the number of endmembers in pixel ($i$, $j$) are appropriately accounted for, $\mathbf{F}_{ij}$ should satisfy the following conditions:

$$\sum_{l=1}^{L} \mathbf{F}_l = 1, \text{ and } \mathbf{F}_l \geqslant 0 \tag{2}$$

In practice, it is possible to miss some endmembers leading to large error terms and $\sum_{l-1}^{L} \mathbf{F}_l \neq 1$. It is well known that inversion of equation (1) (i.e. spectral unmixing) can be achieved with an LSS when $K > L$ (e.g. $K = 6$, $L = 3$ or 4 in this study) (e.g. Adams *et al*. 1989, Sohn and McCoy 1997, Maselli 1998). The LSS for $\mathbf{F}_{ij}$ is

$$\hat{\mathbf{F}}_{ij} = \left(\mathbf{M}^{\mathbf{T}}\mathbf{M}\right)^{-1}\mathbf{M}^{\mathbf{T}}\mathbf{DN}_{ij} \tag{3}$$

From an image, endmember spectra matrix $\mathbf{M}$ can be obtained in two ways: (i) the use of spectra from pure pixels; and (ii) the use of fractions of different endmembers for a sample of mixed pixels (no less than $K$) to solve for matrix $\mathbf{M}$ using least squares method. In the latter case

$$\hat{\mathbf{M}} = \mathbf{DN}\ \mathbf{F}^{T}\left(\mathbf{F}\ \mathbf{F}^{T}\right)^{-1} \tag{4}$$

Since the inversion in equation (3) does not guarantee that $\mathbf{F}_{ij}$ in equation (2) is in the range of 0 and 1, it is an unconstrained solution (Gong and Zhang 1999). A constrained solution forces each fraction to fall within the range of 0 and 1. It introduces more errors in the estimation and causes unnecessary difficulties in the analysis of endmember adequacy. Therefore, we used the unconstrained LSS. For those fraction estimates $\hat{F}_l < 0$ and $\hat{F}_l > 1$, we simply set $\hat{F}_l = 0$ and $\hat{F}_l = 1$, respectively, and also normalized all $\hat{F}_l (l = 1,2,...,L)$ to make them sum to 1 after obtaining $\hat{\mathbf{F}}_{ij}$ for every pixel in a TM image. For those fraction estimates $\hat{F}_l$ including the shade fraction ($\hat{F}_4$), we allocated the shade fraction to other endmembers using the following formula,

$$\hat{F}'_l = \frac{\hat{F}_l}{1 - \hat{F}_4}, \qquad l = 1,2,3, \tag{5}$$

where, $\hat{F}'_l$ is the adjusted fraction after removing $\hat{F}_4$.

A feed-forward ANN algorithm was also used for unmixing mixed pixels. Its training mechanism is an error-propagation algorithm (Rumelhart *et al*. 1986, Pao 1989). In a layered structure, the input to each node is the sum of the weighted outputs of the nodes in the prior layer, except for the nodes in the input layer, which are connected to the feature values, or DNs of TM bands in this study. The nodes in the last layer output a vector that corresponds to similarities to each class, or fractions of endmembers within a mixed pixel. One layer between the input and output layers is usually sufficient for most learning purposes.

The learning is controlled by a learning rate and a momentum coefficient that need to be specified empirically. To estimate the fractions of endmembers in a mixed pixel, ANN must be trained first. The training is done by repeatedly presenting training samples (pixels) with known fractions of endmembers. Network training is terminated when the network output meets a minimum error criterion or optimal test accuracy is achieved. The trained network can then be used to estimate the fraction of each endmember in a mixed pixel.

Once $\hat{\mathbf{F}}_{ij}$ is obtained, the appropriateness of LSS or ANN estimation of $\mathbf{F}_{ij}$ can be evaluated by the rms error *RMS* for a pixel:

$$RMS = \sqrt{\frac{1}{K}\sum_{k=1}^{K}\left(DN_k - \sum_{l=1}^{L} M_{kl}\hat{F}_l\right)^2} \tag{6}$$

where $M_{kl}$ is element $k$ (band), $l$ (fraction) of matrix $\mathbf{M}$; $\hat{F}_l$ is estimation of $F_l$ that is fraction $l$ in a mixed pixel. *RMS* is usually used to reflect the validity of a linear unmixing model. A large *RMS* means that either the mixing is nonlinear or the endmembers used are inadequate for a given pixel. Field visits indicate that the scene structure of our study area is simple and we are certain that a small number of endmembers is appropriate. The only factor that could cause a large *RMS* is the shade of the hilly relief in the study area.

If test samples are available, we can calculate the residual error *RE* for a test sample:

$$RE = \sqrt{\frac{1}{L}\sum_{l=1}^{L}\left(F_l - \sum_{k=1}^{K} E_{lk}DN_k\right)^2} = \sqrt{\frac{1}{L}\sum_{l=1}^{L}\left(F_l - \hat{F}_l\right)^2} \tag{7}$$

where $F_l$ is actual fraction $l$ in a test sample. *RE* is a precision indicator for the unmixing results generated by both LSS and ANN. Due to the lack of ground data, few studies have used it (e.g. Settle and Drake 1993).

In this study, image radiometric correction was not undertaken. Endmember spectra extracted from the imagery are most commonly employed in spectral unmixing (e.g. Adams *et al.* 1986, Smith *et al.* 1990). A simple linear radiometric correction based on pseudo-invariant targets proved unhelpful in linear unmixing (Gong *et al.* 1994). In a companion paper, another simple radiometric correction of Rayleigh scattering for the same TM image did not improve the crown closure estimation results when various vegetation indices were regressed with crown closure (Xu *et al.* 2003).

## 4. Results and analysis

To reduce the calculation error of fractions, caused by registration errors between the TM imagery and the orthophotographs, we randomly selected each

Table 2. Training and test samples used for this spectral unmixing analysis.

| Samples | With shade | Without shade |
|---|---|---|
| Training | 163 | 86 |
| Test | 82 | 44 |

Table 3. Spectral responding matrices for endmembers: crown closure (f1), grasses (f2), soil (f3) and shaded area (f4), extracted from training samples.

| | f1 | f2 | f3 | f4 |
|---|---|---|---|---|
| **With shade** | | | | |
| TM1 | 66.02 | 86.52 | 86.97 | 65.93 |
| TM2 | 28.89 | 45.03 | 46.20 | 28.32 |
| TM3 | 31.54 | 65.07 | 65.94 | 34.08 |
| TM4 | 82.29 | 73.35 | 78.81 | 47.92 |
| TM5 | 81.01 | 134.51 | 133.25 | 62.64 |
| TM7 | 28.86 | 57.51 | 56.42 | 24.23 |
| **Without shade** | | | | |
| TM1 | 65.53 | 86.56 | 86.89 | |
| TM2 | 28.47 | 45.07 | 46.12 | |
| TM3 | 30.80 | 65.15 | 65.76 | |
| TM4 | 81.57 | 73.40 | 78.86 | |
| TM5 | 79.37 | 134.67 | 132.98 | |
| TM7 | 28.11 | 57.58 | 56.24 | |

TM pixel in a homogeneous patch of similar pixels as the selected pixel. The samples were divided into a training set and a test set (table 2) with each set containing the pixel spectra and the known fractions of endmembers as determined from the orthophoto.

### 4.1. *Use of unconstrained least squares*

The endmember spectral matrices were first calculated with and without the inclusion of a shade component (table 3). Unmixing results of the TM data were subsequently derived (table 4, figure 3). Values in table 4 are fractions in percentage for crown (f1), grass (f2) and soil (f3), respectively. It can be seen from table 3 that the DN vectors corresponding to f2 (grasses) and f3 (soil) endmembers are very similar, and this can be verified in the interpretation results of the orthophotographs. Spectral confusion between the two endmembers implies that their fractions may not be extracted correctly. One of the endmembers may be redundant and can be dropped. In table 4, f3 with 0 value means that the LSS produces negative values for most pixels. Clearly, this happened when no shade endmember was used. However, since the DN vector for the crown endmember is very different from those of f2 and f3, its estimations for the site look reasonable compared to the interpretation

Table 4. Spectral unmixing results (%) with an unconstrained least squares solution.

| | With shade | Without shade |
|---|---|---|
| f1 | 15.56 | 25.88 |
| f2 | 50.96 | 74.12 |
| f3 | 33.54 | 0.00 |
| rms error | 0.363 | 2.797 |
| tra.s./RE | 163/0.600 | 86/0.758 |
| tes.s./RE | 82/0.686 | 44/0.873 |
| tes.f1.s/RE | 82/0.185 | 44/0.174 |

tra.s./RE, number of training samples/residual error; tes.s./RE, number of test samples/residual error; tes.f1.s./RE, number of test samples/residual error for f1 only.

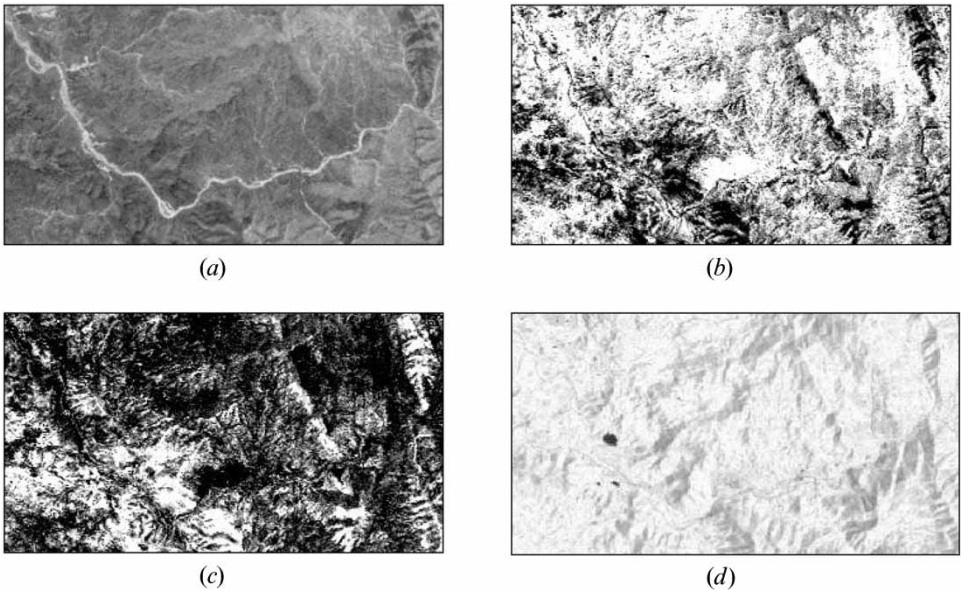


Figure 3. Spectral unmixing results with unconstrained least squares, training samples without the shade endmember: (*a*) crown closure image; (*b*) grass fraction image; (*c*) soil fraction image; and (*d*) rms. error image.

results from the aerial orthophotographs (table 1). Inclusion of the shade endmember in the unmixing led to different fraction results for f1, f2 and f3. Our observation in the field indicates that the shade fraction describing the shaded area in the TM image includes all parts of the other three components with a higher proportion of crown closure because a greater portion of oakwood grows on the shaded side of slopes. The spectral vector of the shade endmember (f4) is more similar to that of crown (f1) (table 3). Therefore, it is not surprising that the inclusion of the shade endmember decreased the crown closure to some extent.

Endmember images (fraction images) and the *RMS* error image generated by LSS are shown in figure 3(*a*)–(*d*). The fraction images were derived by LSS without using the shade endmember. The range of fractions for the three endmembers has been rescaled from [0, 1] to [100, 200]. It can be seen from the f1 image for the site (figure 3(*a*)) that the spatial distribution of fraction of oak crown closure generally agrees with the f1 distribution in figure 2 and its average percentage is close to the value listed in table 1. For f2 and f3 images (figures 3(*b*), (*c*)), the agreement between the fraction images and the interpretation results from the aerial photograph (figure 2) is poor and this can be explained by the spectral confusion between f2 and f3. For the *RMS* error image (figure 3(*d*)), the pixel values were first enlarged ten times, then were subtracted from 255 so that the white areas in the *RMS* image indicate no error and the white to black areas in the image represent varied *RMS* error levels. It can be seen from the error image that the error distribution was related to relief variation, particularly to shade areas, which indicates that unmixing without the use of the shade endmember led to larger *RMS*. The average *RMS* errors are shown in table 4. An average of 0.36 DN (out of 255) with the inclusion of shade endmember and an average of less than 2.8 DN (out of 255) without the

use of the shade endmember were obtained. The error levels are relatively low. The low rms. errors indicate that the model and the number of endmembers used are adequate. Nevertheless, the *RE* levels, calculated from test samples, seem to be high (table 4), especially when unmixing without the shade endmember.

4.2. *Use of ANN*

To train and test the ANN for spectral unmixing, input DNs were first normalized to the range of [0, 1]. The six nodes in the input layer correspond to DNs from TM bands 1–5 and 7. The output layer had three nodes when the shade endmember was excluded and four nodes when the shade endmember was included. They correspond to the fractions in the range of [0, 1]. To find a better ANN structure, we tested various combinations of learning rate ($\eta$), momentum coefficient ($\alpha$) and number of nodes in a hidden layer. We used 86 training samples and 44 test samples, randomly selected from the site without shade endmember. A series of test results from 13 combinations of $\eta$ and $\alpha$ values ($\eta$ varied from 0.1 to 0.8, while $\alpha$ from 0.2 to 0.7) were compared. All *RE*s from test samples varied from 0.22 to 0.28. When using the same input dataset, $\eta = 0.2$ and $\alpha = 0.7$, we assessed the effects of the number of hidden-layer nodes on *RE* calculated from test samples (figure 4). When the hidden-layer nodes were changed from 5 to 50 with various intervals, the lowest *RE* was 0.22 with 9 nodes and the highest RE was 0.25 with 15 nodes. Therefore, we fixed the ANN structure with a 9-node hidden layer and the learning rate $\eta = 0.2$, and momentum coefficient $\alpha = 0.7$.

With the same training datasets as used to derive **M** in LSS, figure 5(*a*)–(*c*) presents unmixing results without shade endmember using the ANN. For the purpose of display, we have used the same rescaling as in figure 3. The distribution of the f1 fraction generated by ANN has a good agreement with the results obtained from photo-interpretation. Higher fraction of crown closure as shown in the f1 fraction image distribute over the eastern part of the image. f2 and f3 fraction

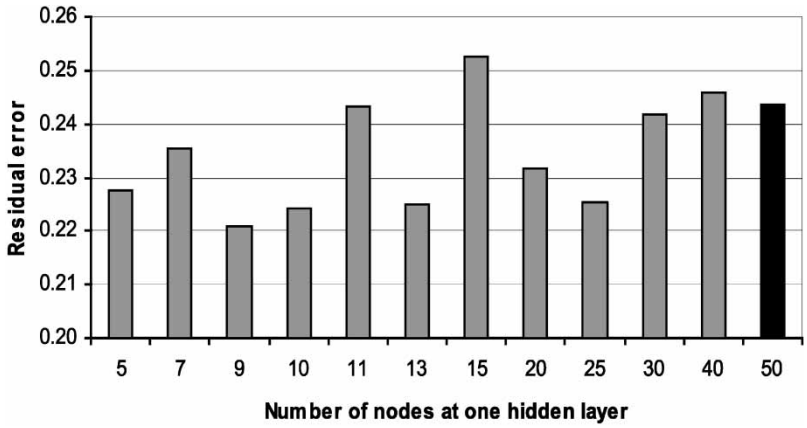


Figure 4. Residual error calculated from test samples with different number of nodes in the hidden layer when fixing the learning rate at 0.2, and the momentum coefficient at 0.7, with 86 training samples and 44 test samples. Unmixing was done without the shade endmember.

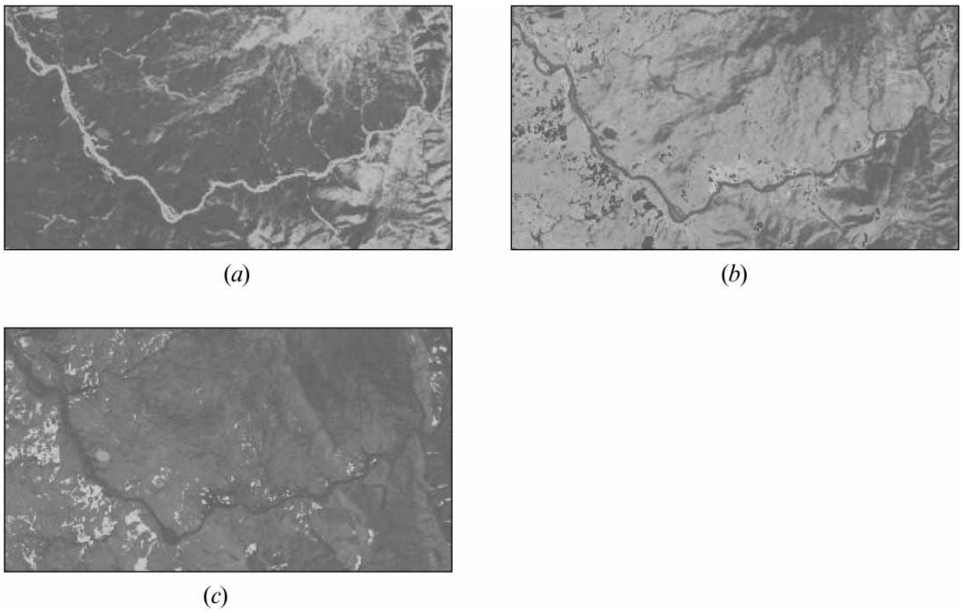


Figure 5. Spectral unmixing results using ANN, without the use of the shade endmember: (*a*) crown closure image; (*b*) grass fraction image; and (*c*) soil fraction image. Learning rate = 0.2, momentum coefficient = 0.7, with a 9-node hidden layer.

images can be separated by ANN and their distributions match those on the orthophoto. This situation is different from figure 3 because ANN can use subtle spectral difference between the two endmembers (Gong *et al.* 1997).

The unmixing results with ANN are summarized in table 5. Without the shade endmember, the best average crown closure was derived with a 9-node hidden layer. The best results are very close to the results interpreted from the orthophotos (table 1). Meanwhile, estimated average fractions for f2 and f3 can be within 10%. The results derived from the inclusion of the shade endmember are poorer than those without it. Since the residual error from the training dataset is not useful for evaluating the ANN's performance (when considering the ANN's overfitting phenomenon), we only list the *RE*s from the test dataset. The average *RE*s in table 5

Table 5. Spectral unmixing results (%) with an artificial neural network algorithm and learning rate of 0.2 and momentum coefficient of 0.7.

| | With shade | Without shade |
|---|---|---|
| Nodes | 9 | 9 |
| f1 | 16.42 | 26.55 |
| f2 | 43.92 | 49.72 |
| f3 | 39.66 | 23.73 |
| tra.s./RE | 163/- | 86/- |
| tes.s./RE | 82/0.115 | 44/0.221 |
| tes.f1.s./RE | 82/0.068 | 44/0.109 |

tra.s./RE, number of training samples/residual error; tes.s./RE, number of test samples/residual error; tes.f1.s./RE, number of test samples/residual error for f1 only.

are lower than those in table 4, both for the average of all endmembers and for the oak crown only. This indicates that the ANN is more effective than the LSS in spectral unmixing.

### 4.3. *Role of the shade endmember*

From the entire study it can be seen that the inclusion of shade in the unmixing analysis can substantially reduce the two unmixing errors, but may result in greater errors in the actual fraction estimation. We attribute this problem partly to the nonlinear topographic effect on the TM imagery and partly to the difficulty in characterizing shade as the sample pixels themselves are mixtures of surface cover altered by illumination. In addition, a higher actual proportion of f1 in the shade area may also cause a greater error in the fraction estimation (see equation (5)). While this requires further investigation, for the purpose of crown closure estimation with the raw TM imagery our results suggest that it is unnecessary to use a shade endmember in a hilly environment like ours.

### 4.4. *Comparison of the two unmixing methods*

In general, the results of crown closure estimation by ANN and LSS can be evaluated from two points. First, the ANN can make use of subtle spectral differences in fraction estimation for those endmembers with similar spectral properties. Therefore, f2 and f3 can be separated by the ANN with a reasonable accuracy (table 5). This cannot be achieved by the LSS (table 4). Second, the ANN can generate a higher estimation accuracy than the LSS as expressed by lower *RE* values and smaller difference between the estimated values from TM data and the interpreted values from the orthophoto, especially for the estimation of crown closure. In summary, based on our experimental results obtained from the study site, the ANN outperforms the unconstrained LSS.

## 5. Conclusions

Few linear mixing studies with TM data use ground data to validate the results of unmixing. We employed land cover classification results interpreted from high resolution orthorectified aerial photographs as ground data to compare two spectral unmixing algorithms.

Based on our experimental results, we conclude that (1) the ANN performs better than the unconstrained LSS when they are used to unmix oak woodland in central California from TM imagery; (2) among the ANNs tested, a three-layer feed-forward ANN structure with learning rate $\eta = 0.2$, momentum coefficient $\alpha = 0.7$ and a 9-node hidden layer performs the best; (3) to estimate oakwood crown closure, a maximum of three endmembers without using a shade endmember is appropriate. The shadow problem caused by topography needs to be resolved before we can make use of the shaded side of the imagery for crown closure estimation.

**Acknowledgments**

This research was partially supported by a NASA land cover and land use grant (NCC5-492).

## References


ADAMS, J. B., SMITH, M. O., and GILLESPIE, A. R., 1989, Simple models for complex natural surfaces: a strategy for the hyperspectral era of remote sensing. *Proceedings of the 1989 International Geoscience and Remote Sensing Symposium*, *Vancouver, BC, Canada* (Piscataway, NJ: IEEE), pp. 16–21.

ADAMS, J. B., SMITH, M. O., and JOHNSON, P. E., 1986, Spectral mixture modeling: a new analysis of rock and soil types at the Viking Lander1 site. *Journal of Geophysical Research*, **91**, 8098–8112.

ALLEN, B. H., HOLZMAN, B. A., and EVETT, R. R., 1991, A classification system for California's hardwood rangelands. *Hilgardia*, **59**, 1–45.

AVERY, T. E., and BURKHART, H. E., 1994, *Forest Measurements*, 4th edn (New York, NY: McGraw Hill).

BARTOLOME, J. W., 1987, California annual grassland and oak savannah. *Rangelands*, **9**, 122–125.

BATESON, A., and CURTISS, B., 1996, A method for manual endmember selection and spectral unmixing. *Remote Sensing of Environment*, **55**, 229–243.

BIGING, G. S., CONGALTON, R. G., and MURPHY, E. C., 1991, A comparison of photointerpretation and ground measurements of forest structure. *Proceedings of the 57th Annual Meeting of American Society for Photogrammetry and Remote Sensing, March, Baltimore, MD* (Bethesda, MD: ASPRS/ACSM), pp. 6–15.

BLUNT, G., SMITH, M. O., ADAMS, J. B., GREELEY, R., and CHRISTENSEN, P. R., 1990, Regional aerolian dynamics and sand mixing in the Gran Desierto: evidence from Landsat Thematic Mapper image. *Journal of Geophysical Research*, **95**, 15462–15482.

BONHAM, C. D., 1989, *Measurements for Terrestrial Vegetation* (New York: John Wiley & Sons).

BOWERS, T. L., and ROWAN, L. C., 1996, Remote mineralogic and lithologic mapping of the ice river alkaline complex, British Columbia, Canada, using AVIRIS data. *Photogrammetric Engineering and Remote Sensing*, **62**, 1379–1385.

DAVIS, F. W., BROWN, R. W., BUYAN, B., and KEALY, J., 1995, Vegetation change in blue oak and blue oak/foothill pine woodland. Contract Report of Forest and Rangeland Resources Assessment Program, California Department of Forestry and Fire Protection, Sacramento, California.

EVANS, J. C., EHRLICH, R., KRANTZ, D., and FULL, W., 1992, A comparison between polytopic vector analysis and empirical orthogonal function analysis for analyzing quasi-geostrophic potential vorticity. *Journal of Geophysical Research – Oceans*, **97**, 2365–2378.

FERRIER, G., and WADGE, G., 1996, The application of imaging spectrometry data to mapping alteration zone associated with gold mineralization in southern Spain. *International Journal of Remote Sensing*, **17**, 331–350.

FOODY, G. M., 1996, Relating the land-cover composition of mixed pixels to artificial neural network classification. *Photogrammetric Engineering and Remote Sensing*, **62**, 491–499.

GONG, P., BIGING, G. S., and STANDIFORD, R., 2000, Technical note. Use of digital surface model for hardwood rangeland monitoring. *Journal of Rangeland Management*, **53**, 622–626.

GONG, P., and CHEN, J., 1992, Boundary uncertainties in digitized maps I: some possible determination methods. *Proceedings of the 1992 Geographic Information System & Land Information System*, *November, San Jose, California* (Bethesda, MD: ASPRS/ACSM), pp. 274–281.

GONG, P., MILLER, J. R., and SPANNER, M., 1994, Forest canopy closure from classification and spectral unmixing: a multi-sensor evaluation of application to an open canopy. *IEEE Transactions on Geoscience and Remote Sensing*, **32**, 1067–1080.

GONG, P., PU, R., and YU, B., 1997, Conifer species recognition: an exploratory analysis of *in situ* hyperspectral data. *Remote Sensing of Environment*, **62**, 189–200.

GONG, P., and ZHANG, A., 1999, Noise effect on linear spectral unmixing. *Geographic Information Sciences*, **5**, 52–57.

HU, Y. H., LEE, H. B., and SCARPACE, F. L., 1999, Optimal linear spectral unmixing. *IEEE Transactions on Geoscience and Remote Sensing*, **37**, 639–645.

LIANG, S., STRAHLER, and LI, X., 1991, Simultaneous inversion of subpixel proportions and signatures of mixed pixels: two components. *Proceedings of the American Congress on Surveying and Mapping & American Society for Photogrammetry and Remote Sensing Fall Convention*, *Atlanta, Georgia* (Bethesda, MD: ASPRS/ACSM), pp. B108–117.

MASELLI, F., 1998, Multiclass spectral decomposition of remotely sensed scenes by selective pixel unmixing. *IEEE Transactions on Geoscience and Remote Sensing*, **36**, 1809–1820.

MCGWIRE, K., MINOR, T., and FENSTERMAKER, L., 2000, Hyperspectral mixture modeling for quantifying sparse vegetation cover in arid environments. *Remote Sensing of Environment*, **72**, 360–374.

PAO, Y., 1989, *Adaptive Pattern Recognition and Neural Networks* (New York: Addison Wesley).

RUMELHART, D. E., HINTON, G. E., and WILLIAMS, R. J., 1986, Learning internal representations by error propagation. In *Parallel Distributed Processing-Explorations in the Microstructure of Cognition*, edited by D.E. Rumelhart and J.L. McClelland, Vol. 1 (Cambridge, MA: MIT Press), pp. 318–362.

SASAKI, K., KAWATA, S., and MINAMI, S., 1983, Constrained nonlinear method for estimating component spectra from multicomponent mixtures. *Applied Optics*, **22**, 3599–3603.

SETTLE, J. J., and DRAKE, N. A., 1993, Linear mixing and the estimation of ground cover proportions. *International Journal of Remote Sensing*, **14**, 1159–1177.

SMITH, M. O., USTIN, S. L., ADAMS, J. B., and GILLESPIE, A. R., 1990, Vegetation in deserts: I. A regional measure of abundance from multispectral images. *Remote Sensing of Environment*, **31**, 1–25.

SOHN, Y., and MCCOY, R. W., 1997, Mapping desert shrub rangeland using spectral unmixing and modeling spectral mixtures with TM data. *Photogrammetric Engineering and Remote Sensing*, **63**, 707–716.

STANDIFORD, R., 1999, Forestry research examines economic pressures facing rangeland owners. *Breakthroughs*, **5**(2), 4–5.

USTIN, S. L., SMITH, M. O., ROBERT, D., GAMON, J. A., and FIELD, C. B., 1992, Using AVIRIS images to measure temporal trends in abundance of photosynthetic and non-photosynthetic canopy components. *Summaries of the 3rd Annual Jet Propulsion Laboratory Airborne Geoscience Workshop*, *1–5 June*, edited by R. O. Green (Pasadena, CA: NASA, Jet Propulsion Laboratory, California Institute of Technology), **1**, pp. 5–7.

WANG, X., and ZHANG, Y., 1998, The study on decompositing AVHRR mixed pixels by means of neural network model. *Journal of Remote Sensing*, **2**, 51–56. (In Chinese.)

XU, B., GONG, P., and PU, R., 2003, Crown closure estimation of oak savannah in a dry season with Landsat TM imagery: comparison of various indices through correlation analysis. *International Journal of Remote Sensing*, **24**, 1811–1822.

ZHANG, L., LI, D., TONG, Q., and ZHENG, L., 1998, Study of the spectral mixture model of soil and vegetation in Poyang Lake area, China. *International Journal of Remote Sensing*, **19**, 2077–2084.